Relationships among seismic velocity, metamorphism, and seismic and aseismic fault slip in the Salton Sea Geothermal Field region

Jeffrey J. McGuire[1], Rowena B. Lohman[2], Rufus D. Catchings[3], Michael J. Rymer[3], and Mark R. Goldman[3]

[1]Department of Geology and Geophysics, MS24, Woods Hole Oceanographic Institution, Woods Hole, Massachusetts, USA, [2]Department of Earth and Atmospheric Sciences, Cornell University, Ithaca, New York, USA, [3]U.S. Geological Survey, Menlo Park, California, USA

Abstract The Salton Sea Geothermal Field is one of the most geothermally and seismically active areas in California and presents an opportunity to study the effect of high-temperature metamorphism on the properties of seismogenic faults. The area includes numerous active tectonic faults that have recently been imaged with active source seismic reflection and refraction. We utilize the active source surveys, along with the abundant microseismicity data from a dense borehole seismic network, to image the 3-D variations in seismic velocity in the upper 5 km of the crust. There are strong velocity variations, up to ~30%, that correlate spatially with the distribution of shallow heat flow patterns. The combination of hydrothermal circulation and high-temperature contact metamorphism has significantly altered the shallow sandstone sedimentary layers within the geothermal field to denser, more feldspathic, rock with higher *P* wave velocity, as is seen in the numerous exploration wells within the field. This alteration appears to have a first-order effect on the frictional stability of shallow faults. In 2005, a large earthquake swarm and deformation event occurred. Analysis of interferometric synthetic aperture radar data and earthquake relocations indicates that the shallow aseismic fault creep that occurred in 2005 was localized on the Kalin fault system that lies just outside the region of high-temperature metamorphism. In contrast, the earthquake swarm, which includes all of the *M* > 4 earthquakes to have occurred within the Salton Sea Geothermal Field in the last 15 years, ruptured the Main Central Fault (MCF) system that is localized in the heart of the geothermal anomaly. The background microseismicity induced by the geothermal operations is also concentrated in the high-temperature regions in the vicinity of operational wells. However, while this microseismicity occurs over a few kilometer scale region, much of it is clustered in earthquake swarms that last from hours to a few days and are localized near the MCF system.

1. Introduction

Faults in the nominally brittle portion of the Earth's crust fail in a wide variety of manners, including earthquake rupture, seismic tremor, continuous creep, and aseismic creep transients. This variety of behaviors suggests that the mechanical processes governing fault failure are complex. For faults in quartz-dominated rocks, the style of slip is thought to be a relatively simple function of temperature and pressure with three distinct regimes: a shallow, velocity-strengthening region (~0–3 km depth) within relatively unconsolidated damage zones where faults creep both continuously and in transient events (often as afterslip), a deeper seismogenic zone where the increased pressure promotes unstable velocity-weakening failure (~3–15 km depth in California), and a deeper ductile region where plate motion is accommodated stably in a wider shear zone due to the activation of deformation mechanisms that dominate at higher temperatures [*Tse and Rice*, 1986; *Marone*, 1998; *Scholz*, 1998]. The upper frictional stability transition is thought to be related to compaction of fault gouge [*Marone et al.*, 1991], whereas the lower brittle-ductile transition is typically thought to occur at around 350°C, coincident with the onset of crystal plasticity in quartz [*Blanpied et al.*, 1991].

Strike-slip faults in the Salton Trough, California (Figure 1), routinely exhibit complex deformation patterns that are not easily explainable in terms of this first-order synoptic model of faults. First, the shallowest, nominally velocity-strengthening layers fail in large creep events [*Brune and Allen*, 1967; *Bodin et al.*, 1994;
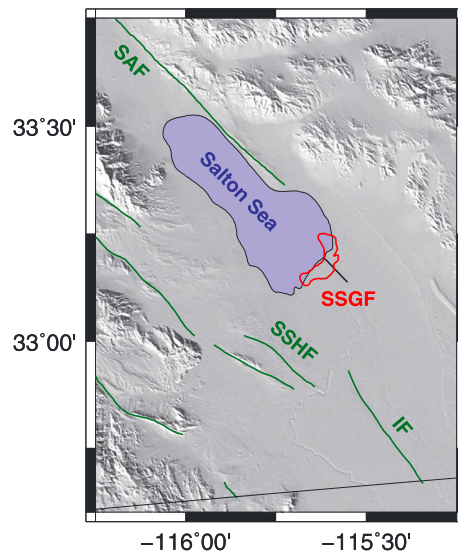
Figure 1. Regional shaded relief map of the Salton Trough area showing the Salton Sea Geothermal Field (SSGF in red) as well as the San Andreas Fault (SAF), Imperial Fault (IF), and Superstition Hills Fault (SSHF) from the Southern California Earthquake Center Community Fault model. Blue shows the location of the Salton Sea.

Bilham et al., 2004; Lohman and McGuire, 2007; Wei et al., 2009] that are clearly instabilities, yet they occur too slowly (hours-days) to radiate seismic waves. At a minimum, the existence of these instabilities requires a significant amount of heterogeneity in the frictional properties of the shallow (~0–3 km) sedimentary rocks [Wei et al., 2013] and possibly more complex failure mechanisms than standard rate-state friction. At least in some cases these creep events are associated with migrating earthquake swarms [Lohman and McGuire, 2007; Roland and McGuire, 2009; Hauksson et al., 2013], which are ubiquitous within the Salton Trough [Richter, 1958; Johnson and Hadley, 1976; Roland and McGuire, 2009], and likely indicate that stressing rates experienced within the seismogenic zone can increase by many orders of magnitude for short time periods [Llenos et al., 2009; Llenos and McGuire, 2011]. Many Salton Trough swarms also show spatial migration rates that are consistent with fluid diffusion, suggesting significant pore pressure transients [Chen and Shearer, 2011].

The combination of well-located background microseismicity, the 2005 Obsidian Buttes swarm, and a recently acquired pair of active source seismic lines that were designed to cross the major faults within the Salton Sea Geothermal Field (SSGF) [Catchings et al., 2010] presents an opportunity to integrate detailed studies of seismic and aseismic slip in the SSGF with a rock mechanics-based model of fault stability. A deeper understanding of the interactions between the induced seismicity and the existing tectonic fault system will likely require models such as these, which include the pronounced spatial gradients in temperature and rock properties within this region. The goal of this paper is to integrate the various seismic observations into a three-dimensional P wave velocity model and to refine the earthquake locations within that model so that they can be directly compared with the faults observed in both the active source lines and geodetic observations of aseismic slip. We will use this suite of approaches to investigate the interactions between induced seismicity and natural seismic and aseismic fault slip on the larger-scale tectonic faults in the SSGF.

1.1. Geologic Setting: The Salton Sea Geothermal Field

The Salton Sea Geothermal Field in the heart of the Salton Trough (Figures 1 and 2) exhibits all of the behaviors described above within the space of a few kilometers, making it a natural rock mechanics experiment occurring within a major plate boundary zone. Here a magmatic intrusion has dramatically altered the thermal structure of the sediments, with the associated hydrothermal alteration causing changes in the dominant mineral assemblages. The existence of the igneous intrusive body is inferred from bulls-eye gravity and magnetic anomalies, high seismic velocities, and a localized temperature anomaly, all of which are coincident with the volcanic centers (Obsidian Butte, Rock Hill, Mullet Island, and Red Island) located along the southern coast of the Salton Sea [Elders and Sass, 1988, and references therein] (Figure 1).

Studies of fault behaviors within the SSGF region also benefit from dense observations of subsurface properties, seismicity, and deformation rates. Numerous shallow geothermal exploration wells and one deep Continental Drilling project well (~3 km) have provided extensive information about the stratigraphy within and adjacent to the geothermal field. In general, the field is overlain by ~500 m of impermeable cap rock, composed of unconsolidated clay, silt, and gravel within which heat flow is high and primarily conductive [Younker et al., 1982]. Between the cap rock and the base of the geothermal wells (typically 1000–2000 m) lies an "upper reservoir layer" of relatively unaltered sandstone with higher porosity and significant fracturing,
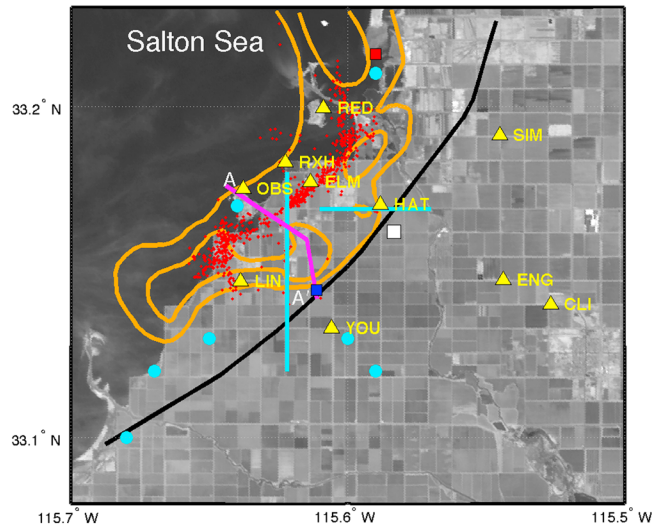
Figure 2. Landsat image of the Salton Sea Geothermal Field. Stations ELM, HAT, LIN, OBS, RED, SIM, YOU, and ENG are from the CalENergy network; RXH and CLI (small triangle next to ELM, short period vertical only) are from the Southern California Seismic Network. The orange contours show the 600°C/km (inner) and 300°C/km (outermost) contours of the shallow geothermal gradient from *Hulen et al.* [2002]. The red dots denote the epicenters of the 2005 earthquake swarm. The white square denotes the location of the 2005 surface break observed by M. Rymer and K. Hudnut (personal communication, 2005). The blue and red squares denote the locations of the Sinclair No. 3 and State 2–14 wells, respectively. The black line denotes the surface trace of the best fit fault plane determined from the inversion of the 2005 InSAR data. The light blue lines denote the active source seismic lines of *Catchings et al.* [2010]. The light blue circles denote the locations of nearby large shots of the SSIP project [*Rose et al.*, 2013] that were recorded on the passive seismic network. The magenta line denotes the A-A′ cross section of *Hulen et al.* [2003] shown in Figure 3.
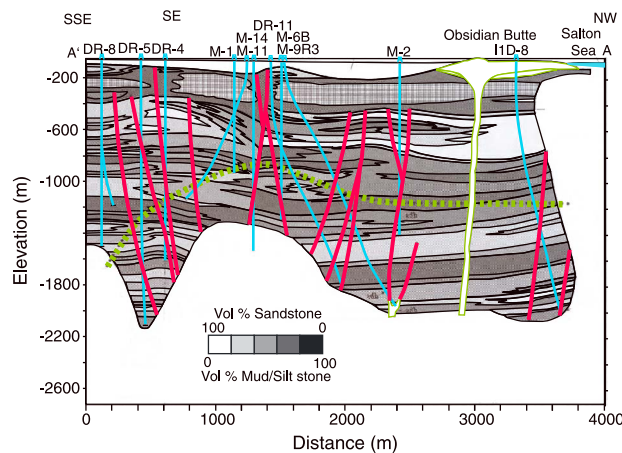
and a "lower reservoir layer" of reduced porosity, hydrothermally altered sediments that have been metamorphosed into dense, highly fractured albite-epidote hornfels [*Clayton et al.*, 1968] (Figure 3). The boundary between the cap rock and the reservoir is associated with a large jump in seismic velocity and a steep geothermal gradient [*Younker et al.*, 1982]. The reservoir is generally defined as the region where the shallow thermal gradient in the 30–80 m depth range exceeds 200°C/km [*Newmark et al.*, 1988; *Hulen and Pulka*, 2001; *Hulen et al.*, 2002]. Some wells reach temperatures as high as 350°C at 2 km depth [*Hulen and Pulka*, 2001]. Thus, in the core of the SSGF, the typical brittle-ductile transition that controls the maximum earthquake nucleation depth should occur at shallower depths than in the rest of California. However, abundant seismicity occurs below this depth, within the metamorphosed sediments of the lower reservoir layer [*Lohman and McGuire*, 2007].

The SSGF is located within a rapidly deforming plate boundary zone, creating a scenario where human-induced perturbations to fluid flow are collocated with a high slip-rate tectonic fault system. Fluid circulation within the reservoir is thought to be dominantly vertical rising of hot fluid (~400°C) along highly permeable fractures and faults. The numerous geothermal wells typically tap into this fluid at depths of 1–2 km (Figure 3). The largest structural feature in the field is termed "the Main Central Fault" (MCF) and is thought to be a 5–10 km long left-lateral strike-slip fault that is a major zone of high permeability and upflow from the deeper reservoir [*Hulen et al.*, 2003]. Deformation is localized near the SSGF both at the present time [*Eneva and Adams*, 2010; *Crowell et al.*, 2013] as well as on geologic time scales [*Brothers et al.*, 2011]. Some of this deformation

Figure 3. After Figure 5 of *Hulen et al.* [2003]. Geologic cross section through the western part of the SSGF along the A to A′ line shown in Figure 2. Gray scale colors represent lithology ranging from 100% (white) to 0% (black) sandstone (see *Hulen et al.* [2003] for details). Individual geothermal wells are shown in light blue and labeled along the top. Major faults interpreted by *Hulen et al.* [2003] are shown in red. The dashed green line denotes the upper limit of the geothermal reservoir (roughly 275°C). The Main Central Fault consists of multiple strands that intersect the surface near wells DR-11 and M-6B.

occurs seismically in both large earthquake swarms on tectonic faults [*Lohman and McGuire*, 2007] and in multiple clusters of induced seismicity associated with the geothermal field [*Chen and Shearer*, 2011; *Hauksson et al.*, 2013]. A pronounced increase in earthquake stress drops with distance from the nearest injection well suggests that the geothermal wells influence the ambient stress field and indicate an increase in fluid pressure that decays over a length scale of approximately 2 km from a given well [*Chen and Shearer*, 2011]. Recently, it has been suggested that there is a nontrivial probability that the induced seismicity associated with geothermal power production could trigger an earthquake on nearby large faults, most notably the southern San Andreas [*Brodsky and Lajoie*, 2013]. However, this initial study was based on the extrapolation of statistical models without a detailed analysis of the geologic structures within the SSGF. The relationships described below indicate that pronounced variations in material properties exist within the SSGF and profoundly affect the allowable behaviors on faults and accommodation of strain within the region.

1.2. Deformation and Seismicity Observed During 2005 Swarm

The 2005 earthquake swarm demonstrated that the larger faults within the SSGF were indeed able to fail in damaging, $M > 5$ events. Deformation during the 2005 swarm was observed with interferometric synthetic aperture radar (InSAR) and GPS; an inversion of these data indicates that the geodetic signal was dominated by slip (Mw ~5.7) in the upper ~3 km [*Lohman and McGuire*, 2007]. This aseismic slip was both larger in moment (Mw ~5.7 versus Mw ~5.3) than the moment release due to seismicity alone and occurred within a shallower depth range that did not overlap with the seismicity. Precise relocations of the swarm earthquakes with a regional velocity model demonstrated that they occurred primarily in the 3–5 km depth range [*Lohman and McGuire*, 2007]. Thus, at around 2–3 km depth, there is a transition from velocity-strengthening fault friction (0–~3 km) to velocity-weakening friction (3–6 km).

In some ways this variation of behavior with depth is not a surprising result; continental strike-slip fault zones typically are associated with a shallow velocity-strengthening layer that does not produce much slip in major earthquakes [*Fialko et al.*, 2005]. However, connecting the spatial separation between seismic and aseismic slip in the 2005 swarm with models of frictional stability based on laboratory rock mechanics is challenging, given the steep geothermal gradients at this site. Nearby geothermal wells indicate that temperatures reach ~350°C by ~2 km depth [*Hulen and Pulka*, 2001]. The aseismic nature of the upper ~2 km likely reflects both the effects of increasing consolidation and normal stress with depth [*Marone et al.*, 1991], as well as the velocity-strengthening nature of quartz-dominated rocks at these elevated temperatures expected from laboratory experiments [*Blanpied et al.*, 1991]. In contrast, the temperatures where the earthquakes occurred are likely well out of the range where frictional instability and earthquakes should occur in quartz-dominated/granitic materials [*Blanpied et al.*, 1991].

1.3. The Obsidian Creep Active Source Experiment

In 2010 we undertook a high-resolution active source seismic reflection/refraction experiment aimed at identifying the locations of the major tectonic fault systems within the SSGF [*Catchings et al.*, 2010]. The survey consisted of a 6 km long, N-S line in the western part of the field and a 3 km long, E-W line in the vicinity surface faulting associated with the 2005 swarm (Figure 2). The migrated seismic sections from each line from *Catchings et al.* [2010] are shown in Figure 4. Both the N-S and E-W lines crossed numerous active faults. In particular, the N-S line found a region of multiple vertical fault strands in the distance range from 4000 to 5000 m (Figure 4) that corresponds with the Main Central Fault zone identified by *Hulen et al.* [2003] from well data (Figure 3). The E-W line also found multiple active faults that collectively show a trend of vertical offsets that result in down dropping of the SSGF region (Figure 4). The largest of these offsets (at meter 3000 of the seismic line) occurs very close to the surface trace of the fault scarp identified by field surveys following the 2005 swarm (M. Rymer and K. Hudnut, personal communication, 2005).

The N-S line included shots every 40 m that were timed with GPS and varied between 0.15 kg (1/3 lb) and 0.90 kg (2 lb) [*Catchings et al.*, 2010]. This line followed Boyle Road. Fortunately during the time of our experiment, the local borehole seismic network, operated by the geothermal plant operator, CalEnergy Inc., made its data available to the public free of charge through the Southern California Seismic Network (SCSN), which greatly increased the density of available data for both earthquakes and shots in the region (Figure 2). The larger shots from the N-S line were well recorded on multiple stations of the CalEnergy seismic network (Figure 2). The E-W line used smaller Betsy Seisgun® shots that were not recorded at large
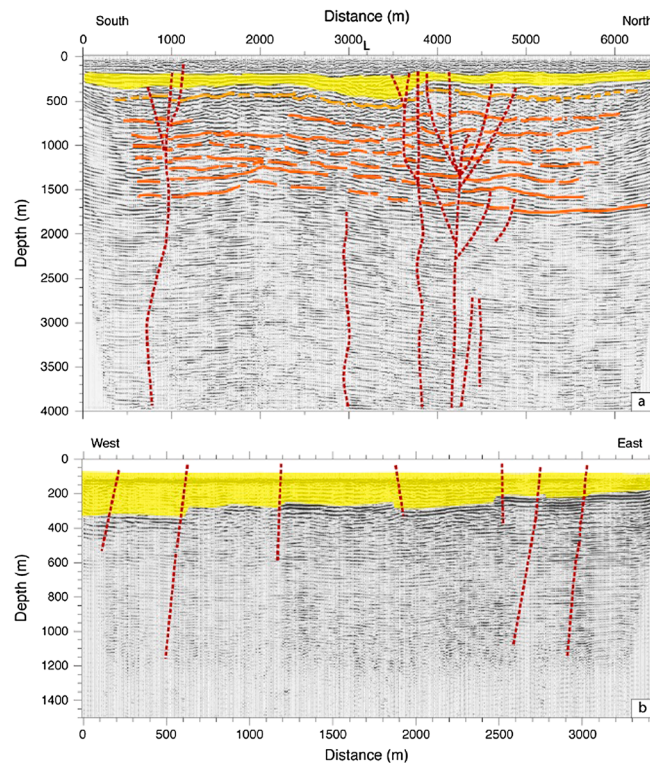
Figure 4. Seismic sections for the (a) N-S and (b) E-W active source lines with interpreted faults from *Catchings et al.* [2010]. Some of the interpretative faults are shown as dashed lines. Laterally continuous stratigraphic units are shown in shades of yellow, brown, and orange. The L in Figure 4a denotes where the profile crosses Lindsey road.

offsets [*Catchings et al.*, 2010]. The N-S line resolved extremely strong variations in *P* wave velocity over distances of only ~2 km. The *P* wave velocities were roughly 20% higher in the geothermal field in the upper 1–1.5 km depth range than just outside the field. This high-velocity anomaly likely reflects the high-temperature metamorphism of the Salton Trough sediments above the intrusive magma body. Unfortunately, the refraction-derived velocity model from line 1 only has resolution down to about 1.5 km depth and hence does not reveal the extent to which the strong velocity anomalies continue into the seismogenic zone. Additional active source data are available from the larger-scale Salton Seismic Imaging Project (SSIP) [*Rose et al.*, 2013], which included several large borehole shots within our study region that were recorded on all seismometers of the CalEnergy network. In this study, we combine the *P* wave traveltimes from the active sources as recorded on the CalEnergy and SCSN stations with arrival time data from the abundant local seismicity in an attempt to resolve the three-dimensional velocity structure of the SSGF and to relocate the seismicity within the three-dimensional structure.

2. Data

To jointly determine the (*P* wave) velocity structure and precise earthquake locations, we utilize the tomoDD method to solve for both in an iterative manner [*Zhang and Thurber*, 2003, 2006]. We use three types of traveltime measurements in the tomoDD inversion for earthquake locations and velocity structure. We picked arrivals from 140 shots on the N-S line that were visible at the CalEnergy stations, as well as seven larger shots within our study region from the SSIP experiment. Shots from the N-S line were typically picked at 2–5 stations, whereas the larger SSIP shots were typically picked across the entire 10 station array. This resulted in a total of 447 absolute traveltime picks. These were treated as absolute traveltimes in the tomoDD inversion framework, allowing them to be weighted strongly owing to their known source location and origin time. The absolute traveltimes are shown in Figure 5 as a function of distance from the shot. There is roughly a 30–50% variation in traveltime for different shots at a particular distance, indicating that our data set samples the large-magnitude variations seen in the N-S line but over the broader area covered by the seismic network.

For earthquake-derived data, we utilized a catalog of 2330 earthquakes that occurred between December 2007 and February 2012. Differential arrival time values for *P* and *S* waves were calculated from the first-arrival picks made by the Southern California Seismic Network. These catalog differential times were utilized in the inversion for event pairs with at least eight phase pairs in common. We calculated waveform differential time picks using a time window extending from 0.7 s before to 1.86 s after the catalog arrival time picks. Both *P* and *S* waveforms were band-pass filtered between 3 and 12 Hz. Waveform differential times were utilized in the inversion for all event pairs which had at least five phases (*P* and/or *S*) with correlation coefficients $> = 0.75$.
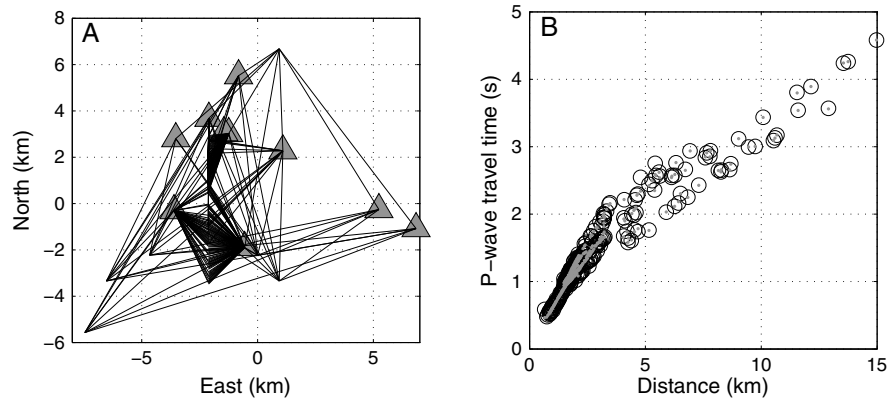
Figure 5. (a) Map view of 1-D raypaths for active source shots recorded at the seismic network (gray triangles). Shots from *Catchings et al.* [2010] lie on a N-S line at −2 km east; the wider distributed shots are from the SSIP experiment [*Rose et al.*, 2012]. The X,Y zero coordinate is at 33.15°N, 115.6°W. The local X,Y coordinate system is used in the text and subsequent figures. (b) Absolute P wave traveltime picks from active source shots at the CalEnergy network seismic stations (black circles) and the fit to them for the final 3-D Vp model (gray dots).

3. Inversion Results

The inversion started with the following numbers of each data type: 73,070 cross-correlation P differential times, 71,786 cross-correlation S differential times, 124,973 P catalog times, 15,171 S catalog differential times, and 411 absolute P wave traveltimes from a total of 2328 earthquakes. The input velocity model was defined on a grid with variable spacing overall but a uniform 500 m spacing within the area with the highest station/earthquake densities (roughly −5 to 5 km in both x and y in Figure 6). The spacing of nodes in depth was variable, increasing from 300 m in the shallowest model (<3.5 km) to 600 m in the lower crust. The data weighting and residual threshold scheme used in the inversion are given in Table 1. The model smoothing values were set to 15 in the x, y, and z directions based on the results of the resolution test discussed below. The first six iterations of the inversion solved only for changes to the velocity structure, while iterations 7–12 solved for both changes to velocity structure and earthquake locations. After 12 iterations, 100% of the events, 85% of the cross-correlation times, and 84% of the catalog times were retained. Condition numbers for the individual iterations were in the 50–75 range. Figure 5 shows the fit to the active source data, which is
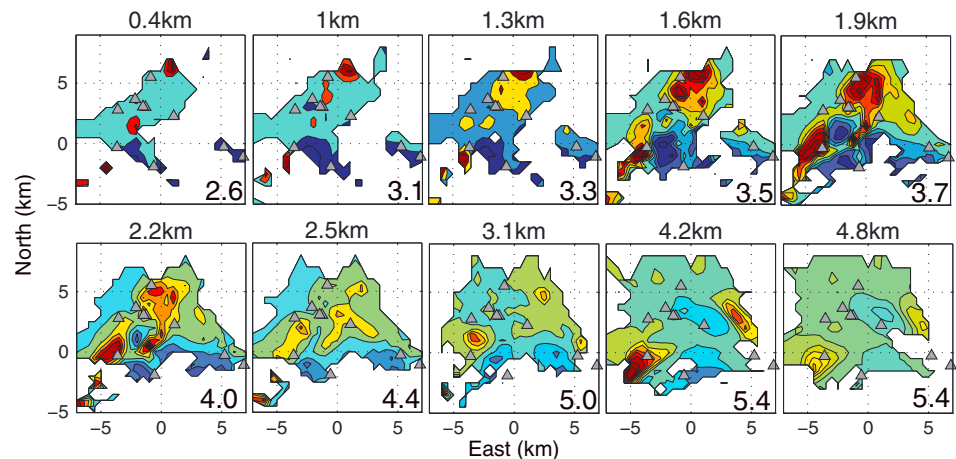

Figure 6. Final 3-D velocity model. The panels show the velocity model at different depth slices. The median P velocity at each depth is shown in the lower right corner of each panel in units of km/s. The color scale varies from panel to panel, ranging from 20% faster (red) to 20% slower (blue) than the median velocity at that depth. The model is masked to show only the regions where the DWS ≥ 1.0. The X and Y coordinates are in kilometer, with the origin at 33.15°N, 115.6°W. The triangles show the locations of the seismic stations as in Figure 2.

Table 1. TomoDD Relocation Parameters[a]

	Cross-Correlation Data		Catalog Data			
Iteration	P Wave Weight	S Wave Weight	P Wave Weight	S Wave Weight	Absolute/Differential Ratio	DWS Threshold
1–6	1.0	1.0	0.75	0.75	100	0.5
7–12	0.8	1.0	0.4	0.4	100	0.5

[a]Iterations 1–6 only inverted for changes to the velocity structure, while iterations 7–12 determined both velocity structure and earthquake relocations. All distance cutoffs for differential times were set at 3 km.

in general quite good (due to the high weighting of these data) and indicates that our velocity model has recovered the full range of variability seen in the traveltimes for a given offset.

Figure 6 presents the estimated Vp model at a range of depths from the surface to about 5 km in depth. Only the areas of the model where the derivative weight sum (DWS) is greater than 1 are shown. This threshold roughly describes the portions of the model where a checkerboard resolution test, described below, was successful. At depths shallower than 1 km, we only have resolution directly under the seismic stations. Thus, we concentrate on the 1–5 km depth range, where our resolution is greatest and where the bulk of the seismicity is located. The predominant feature is very strong fast-velocity anomalies in the 1–3 km depth range for two ~4 km wide regions corresponding to the actively operating parts of the SSGF. These regions are about 30–40% faster than the area between them and the area to the south outside of the field. Figure 7 shows a comparison of the P velocities at 1.9 km depth with the regions of peak geothermal gradient determined from numerous exploration wells [*Hulen et al.*, 2002]. These regions of high shallow geothermal gradient are indicative of the regions of highest heat flow even after accounting for variations in conductivity and other factors [*Newmark et al.*, 1988]. There is a clear overall contrast between high velocities within the SSGF compared to regions just outside it to the SE. There is also suggestions of significant variations of P velocity on the scales of just ~1–2 km within the SSGF that correlate with the heat flow distribution and may be real features as well, though such small features may be below our resolution limit, given the station distribution.

Figure 7. The final P wave velocity model (colors show velocity in km/s). at 1.9 km depth masked to DWS values > 1. The black lines show the 600°C/km (inner) and 300°C/km (outermost) contours of the shallow geothermal gradient from *Hulen et al.* [2002]. Gray triangles show the locations of the seismic network stations.

3.1. Comparison With Well Logs

Figure 8 compares our 3-D velocity model with two available well logs from the SSGF. The State 2–14 well was drilled in 1985 as an academic experiment located in the high heat flow bulls-eye in the northern part of the SSGF (Figure 2). Hence, it is well characterized in terms of both mineralogy and physical properties (see *Elders and Sass* [1988], and references therein). The red curve displays the P wave velocity profile determined in the State 2–14 well using the vertical seismic profiling technique [*Daley et al.*, 1988]. The relatively high velocities (~4.5 km/s at 1.5 km depth) indicate the alteration of the Salton Trough sediments into denser, stronger rock. Also shown is the well log from the Sinclair No. 3 well drilled by Western Geothermal Inc. (blue curve) [*Lovely et al.*, 2006]. This well lies just outside the high heat flow region of the SSGF (Figure 2) and represents relatively unaltered sediments (~3.0 km/s at 1.5 km depth). Also shown in Figure 8 are the one-dimensional
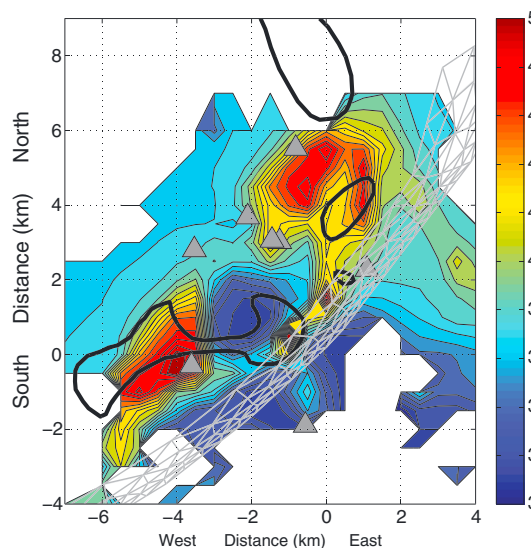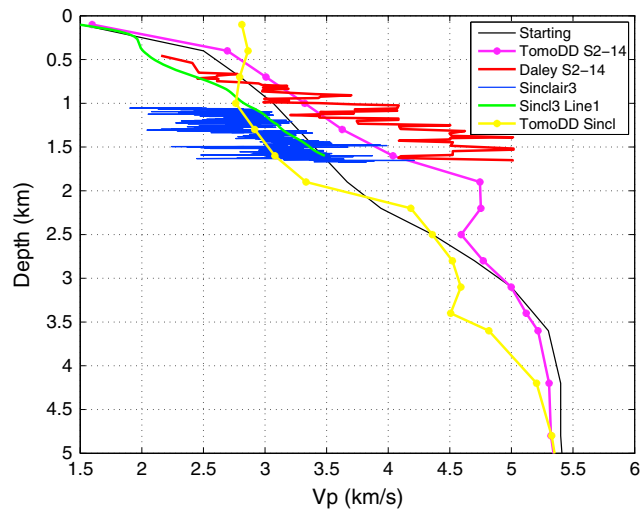
Figure 8. One-dimensional *P* wave velocity profiles from the SSGF. The Sinclair No. 3 (blue from *Lovely et al.* [2006]) and the State 2–14 (red from *Daley et al.* [1988]) wells show the contrast between relatively unaltered and highly altered sediment sections, respectively. The starting model for tomoDD modeling (black) is shown along with two profiles from the 3-D model representing the location of the Sinclair (yellow) and the State (magenta) wells. Note that the magenta curve is actually taken from a model node 2 km south of the State 2–14 well, due to ray coverage limitations. The green curve shows the velocity model derived from the N-S active source line data as presented in *Catchings et al.* [2010].

velocity model we used to initialize the tomoDD algorithm (black line) and two one-dimensional profiles from the resulting three-dimensional model representing the well locations. The magenta profile shows our recovery of the State 2–14 high-velocity region. It is taken from the center of a high-velocity anomaly in the northern part of our velocity model ($x = 0$, $y = 5$ km in Figure 7) instead of the exact State 2–14 location ($x = 1$ km, $y = 7$ km in Figure 7) because the State 2–14 location is located just north of our region of good ray coverage. The yellow profile in Figure 8 shows our 3-D model for the closest node to the Sinclair No. 3 well. It shows good agreement in the 1 to 1.7 km depth range, where the well log data are available. Figure 8 also shows a 1-D profile taken from the closest part of the N-S refraction line to Sinclair No. 3 (Green line, taken from the Vp model of *Catchings et al.* [2010]).

It shows similarly good agreement with the Sinclair well log. The difference between the three-dimensional velocity model (yellow) and the refraction model (green) indicates the lack of resolution at depths shallower than ~1 km for our 3-D model as a consequence of the station spacing. Overall, the 30–40% difference in velocities between the high- and low-heat flow portions of the 3-D model is in good agreement with the available well logs. The comparison with the well logs indicates that we may slightly underestimate the magnitude of the lateral variations in our 3-D model (up to ~40%) that occur within the SSGF area over distances of just a few kilometers.

3.2. Earthquake Relocations

The seismicity from 2008 to 2012 within the SSGF that is relocated as part of the tomoDD inversion occurs primarily in three clusters (Figure S1) as has been seen in both the original SCSN locations and several previous relocation studies [*Lin et al.*, 2007]. Despite abundant waveform differential arrival time measurements, these three clusters do not collapse to a single fault-like structure but instead remain as cloud-like clusters of 2–4 km in scale. Event locations are spatially and temporally related to clusters of injection wells (discussed below). We also used our 3-D velocity model to improve the locations of the 2005 earthquake swarm. We fixed the velocity structure to the 3-D model from above and utilized the differential arrival times from *Lohman and McGuire* [2007] with tomoDD, solving for just the 2005 swarm locations. The station coverage is considerably poorer in 2005, as the CalEnergy network data were not publically available at that time, and hence, the relocation relies primarily on the more broadly distributed set of stations from the Southern California Seismic Network. The relocated 2005 swarm shows the same NE-SW striking, ~5 km long fault that was observed by *Lohman and McGuire* [2007]. This complicated structure has multiple strands at both ends where the faults appear to curve in regions that are coincident with the locations of high heat flow zones (Figure S1).

3.3. Resolution Tests

To evaluate the resolution of our inversion results, we performed a checkerboard test. The input velocity model consisted of a grid of cubes, 3 km on a side (including in depth). Their velocities were perturbed ±10% relative to the 1-D starting model in Figure 8. Synthetic data were calculated for all of the traveltimes in the real data set. Five depth slices of the input *P* wave model are shown in the left hand column in Figure S2.
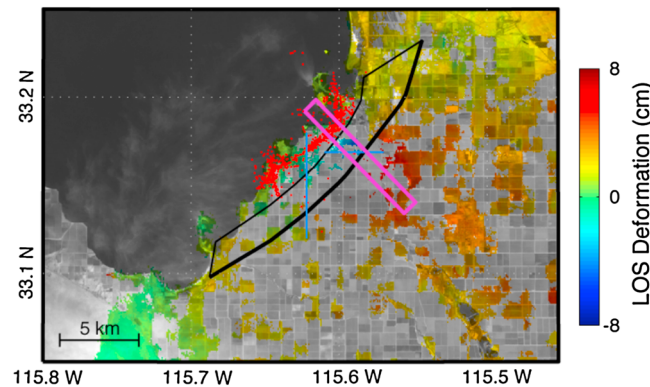
Figure 9. Map of the best fit curved fault (black polygon, heavy line indicates surface trace) and InSAR-derived LOS displacements (background color) associated with the 2005 swarm. The light blue lines denote the active source seismic lines, and the red dots denote the epicenters of the 2005 swarm. The magenta box denotes the NW-SE profile shown in Figure 12.

The four right-hand columns show the recovered velocity model at each corresponding depth for a range of spatial smoothing values applied in four different inversion tests. Cases were run for four different values of the velocity model smoothing parameter (5, 15, 30, and 60) to determine which value was most appropriate for our data set. We kept the smoothing parameter the same in all three spatial dimensions. Smoothing values of 5 or 15 recover the input signal well in our target depth range between 1 and 4 km, whereas higher values of the smoothing parameter damp out the signal. For these values of smoothing, the results indicate that ~10% velocity anomalies that are ~3 km in dimension are well resolved in the 1–4 km depth range; we concentrate in this depth range for this study because that is where the bulk of the seismicity occurs. We do not have good resolution shallower than 1 km, owing to the station spacing of the seismic network and the shots occurring primarily on one N-S line.

3.3.1. Comparison With Geodetic Data

The relocated 2005 epicenters occur approximately 2 km to the north of the fault plane used to invert the InSAR data of *Lohman and McGuire* [2007], even accounting for the northward dip of the fault plane. If robust, this separation further illustrates the spatial heterogeneity of material properties within the SSGF. Here we explore the possibility that the InSAR data could be explained by a fault that is also consistent with the seismicity and steep structures observed during the active source experiments. We reprocessed the InSAR data using a higher-resolution digital elevation model (15 m, National Elevation Database) and employed a time series approach that ingested all available synthetic aperture radar (SAR) imagery over the region to aid in the masking of water, fields, and other regions where perturbation of the land surface between images degrades the SAR data quality (decorrelation) to the point where it became unusable for deformation studies [e.g., *Lyons and Sandwell*, 2003]. SAR interferograms measure changes in the distance between the satellite and the ground within the line of sight (LOS) direction of the satellite. The LOS length change is observed as fractions of a wavelength, not in terms of absolute distance between the satellite and the ground. Therefore, a key step in InSAR processing is phase unwrapping, which resolves the 2π jumps present within the data and allows for measurement of relative deformation within the interferogram as a whole. When isolated patches of coherent data are surrounded by regions that are decorrelated, due to agricultural activity or other processes, it can be challenging to constrain the appropriate number of cycles required to connect to the rest of the interferogram. Our reprocessing of the data highlighted a few small regions immediately adjacent to the highest gradients in deformation, where the appropriate number of cycles to use in phase unwrapping was ambiguous. Therefore, we performed inversions where we allowed these regions to vary by integer number of 2π cycles relative to the rest of the interferogram. These perturbations resulted in only minimal variations in inferred slip at the very shallowest (<100 m) portions of the fault.

The resulting deformation field is shown in Figure 9, along with the locations of the seismic lines, microseismicity, and the best fitting curved fault surface from inversion of the InSAR data. The best fitting fault intersects the surface in the middle of our E-W seismic line, about 2.5 km SE of the 2005 swarm relocations and coincident with the surface break observed in 2005 by M. Rymer and K. Hudnut (personal communication 2005). Whereas the best fitting fault plane does dip slightly to the NW, it does not intersect the 2005 swarm relocations. Moreover, it intersects the N-S seismic line approximately 3 km south of the zone of intense near-surface faulting as seen in the seismic lines (Figure 4). Thus, the best fitting plane for the InSAR data does not appear to be coincident with the Main Central Fault but is consistent with the large offset
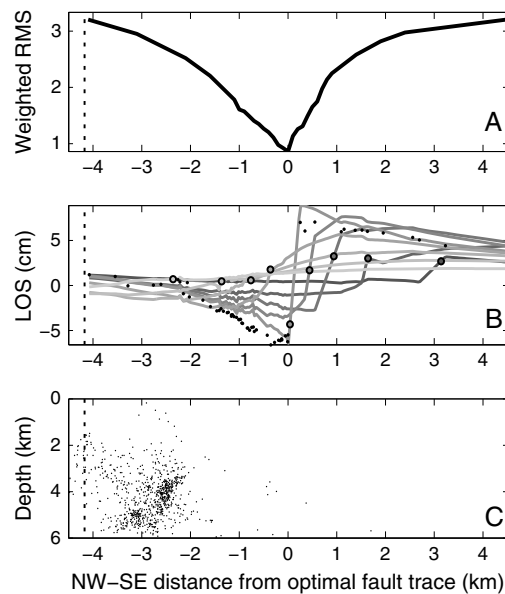
Figure 10. Effect of shifting fault along NW-SE profile. (a) Weighted residual norm for shifts of the fault—0 km is at the location of our best fit fault (Figure 9). Salton Sea shoreline is shown by dotted line. (b) Line of sight (LOS) observations along profile in Figure 9 (black points) and predicted displacements (gray scale) for shifted faults, with surface trace location for each shifted model shown by filled circles for each curve. (c) The 2005 swarm seismicity (black dots) along the same profile as Figures 10a and 10b.

steeply dipping faults observed in our E-W line [*Catchings et al.*, 2010], including the recently mapped Kalin fault [*Rymer et al.*, 2010].

To verify that the InSAR data could not be satisfied by a fault that intersects the swarm at the depth of seismicity and that has the steep dip of structures observed along the seismic lines, we performed a series of inversions where we shifted the fault plane in the NW-SE direction perpendicular to the fault. Figure 10a shows the degradation of the fit to the InSAR data as the source fault is moved in the NE or SW direction relative to the plane shown in Figure 9. At each location, we inverted the full set of InSAR data for a new distribution of slip and show the prediction and fit to data within the profile crossing the peak deformation and densest seismicity (box, Figure 9) In particular, the 3 km shift to the northwest that would be required to place the fault surface above the seismicity results in about a factor of 3 incre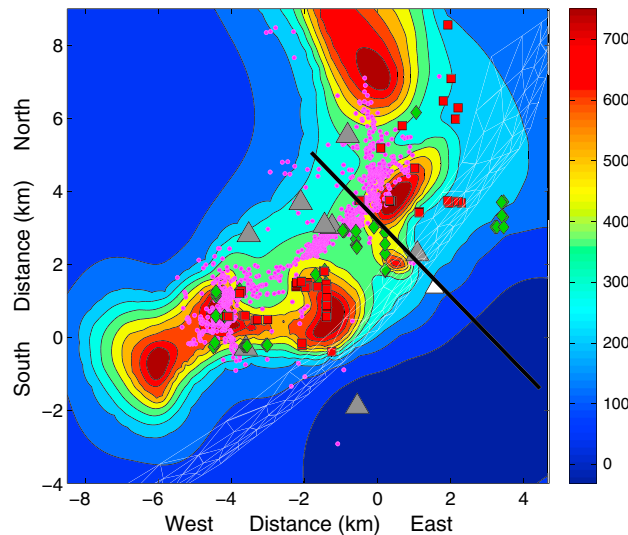ase in the residuals (Figures 10a and 10b). The LOS displacements are dominated by a clear discontinuity that is in the vicinity of the Kalin fault and cannot be matched with shifts of more than ~100 m from the optimal plane shown in Figure 9.

4. Discussion

4.1. The 2005 Swarm and Main Central Fault Zone

The 2005 earthquake swarm appears to have ruptured the Main Central Fault zone of *Hulen et al.* [2003]. The Main Central Fault zone is complicated in that, at shallow depths, it clearly involves multiple fault strands even in its most planar section (Figure 3). The NE-SW striking fault segment is ~8 km long and connects two regions of extremely high thermal gradient. Figure 11 illustrates how both the NE and SW terminations of the fault occur in bulls-eye regions where the shallow thermal gradient exceeds 600°C/km. At both terminations, the trend of the 2005 seismicity bends and continues ~1–3 km on NNW-SSE striking faults. These bends in the fault are coincident with intense clusters of background seismicity observed from 2008 to 2012 (Figure S1). In the *Hulen et al.* [2003] cross section (Figure 3), the Main Central Fault zone outcrops at the surface in the vicinity of wells M-11, DR-11, and M-6B (locations in Figure S1) and involves at least two strands, dipping to the SSE and NW, respectively. Our N-S seismic line passes immediately adjacent to these wells, at meters 4900–5000 of the seismic line coordinate system of *Catchings et al.* [2010]. There are numerous near-vertical fault strands visible in the 0–4 km depth range of the migrated section from the N-S line with most occurring near meter 5000 (Figure 4), a few hundred meters to the south of the well cluster [*Catchings et al.*, 2010]. Our relocations of the 2005 swarm intersect the N-S line about 600 m north of the well cluster. Based both on our relocations and on the centroid estimate for the main shock [*Tape et al.*, 2009], the 2005 swarm was concentrated between 3.5 and 5.5 km depth. Therefore, the 600 m offset to the north relative to the well locations in Figure S1 could easily be due to a slight dip (~5° off vertical) to the NW of the Main Central Fault zone, or it could indicate the degree of bias that remains in our earthquake locations, despite the 3-D velocity model attempting to account for the high velocities beneath the SSGF. The sharpness of the fault at depth, as illuminated by the 2005 relocations (Figure 9), along with the numerous shallow faults seen in the *Hulen et al.* [2003] cross section (Figure 3) and our migrated reflection section

Figure 11. Comparison of the best fit fault geometry from the InSAR data (gray mesh) with the shallow temperature gradients in the ~0–500 m depth range corresponding to the conductive cap above the reservoir from *Hulen et al.* [2002]. Colors denote the temperature gradient in °C/km. Injection wells in the geothermal plants are shown as green diamonds, extraction wells are shown as red squares. Seismic stations and the 2005 earthquake swarm are denoted by gray triangles and magenta dots, respectively. The white triangle denotes the surface break observed at the time of the 2005 swarm (M. Rymer and K. Hudnut, personal communication, 2005). The black line denotes the location of the InSAR data cross section in Figure 10 and the Vp cross section in Figure 12. The predominately aseismic slip observed by InSAR in 2005 occurred outside the high-temperature zone, whereas the seismic component of the 2005 swarm occurred on a set of long-term tectonic faults that connect the high-temperature regions.

(Figure 4) [*Catchings et al.*, 2010], suggests that the tectonics of the region may be accommodated by a relatively narrow fault zone at depths >3 km, below a more diffuse flower structure. The Main Central Fault is important both as a left-lateral relay structure in the San Andreas system and also as a primary pathway for rising hot fluids in the geothermal reservoir [*Hulen et al.*, 2003]. In particular, zones of fault breccia that appear to form in fault jogs may have the highest permeability [*Hulen et al.*, 2003].

4.2. Connections Between Seismic and Aseismic Slip in the 2005 Swarm

Lohman and McGuire [2007] assumed that the 2005 earthquake swarm occurred on the deeper extension of the fault inferred from the InSAR data. Given the improved accuracy of the earthquake relocations in this study, the numerous candidate faults identified in the two seismic lines [*Catchings et al.*, 2010] and the reevaluation of the InSAR data
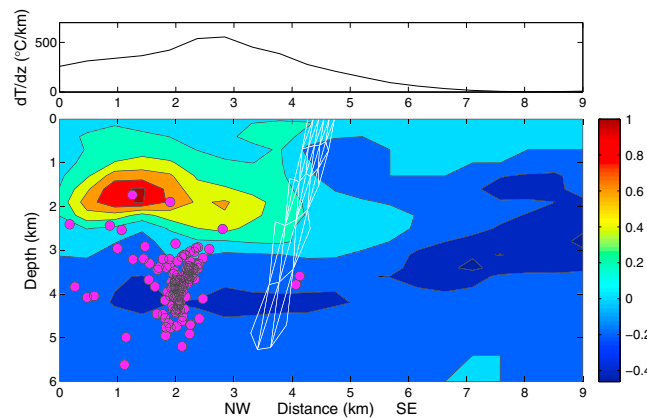
described above, this does not appear to be the case. The LOS displacements show a clear discontinuity that is in the vicinity of the Kalin fault and cannot be matched with shifts of more than ~100 m from the optimal plane shown in Figure 10. Therefore, we conclude that the majority of shallow aseismic creep observed in 2005 occurred on the Kalin fault. Similarly, the 2005 swarm relocated in the three-dimensional velocity model is nearly coincident with the Main Central Fault seen in the active source seismic lines and the geological cross sections (Figures 3 and 4). Thus, the aseismic creep, which is larger in total moment, appears to have occurred both at shallower depths and on a different fault than the earthquake swarm. This spatial partitioning of seismic and aseismic deformation appears to be related to the lithology of the faults. Figure 11 shows the locations of the seismic and aseismic slip faults relative to the temperature gradient map of *Hulen et al.* [2003]. Figure 12 shows a cross section through the velocity model along the line shown in Figure 11. The 2005 seismic slip happens in the heart of the geothermal anomaly and where there are high *P* velocities, whereas the aseismic slip occurred just outside this region in the relatively unaltered sediments.

4.3. Relationships Between Sediment Metamorphism and Frictional Stability

The upper frictional stability transition is thought to be related to compaction of fault gouge [*Marone et al.*, 1991], whereas the lower brittle-ductile transition is typically thought to be temperature controlled. In quartz-dominated rocks, it is thought to occur at around 350°C, coincident with the onset of crystal plasticity [*Blanpied et al.*, 1991]. In contrast, gabbroic samples show velocity-weakening friction behavior up to much higher temperatures, roughly 500–600°C [*He et al.*, 2007]. This higher temperature range for unstable faulting results from the predominance of plagioclase (Pl) and pyroxene (Px) [*He et al.*, 2013]. Even a small amount of quartz contamination (2–5%) can shift a Pl-Px mixture from velocity weakening to velocity strengthening [*He et al.*, 2013]. Given that temperatures reach ~350°C by ~2 km depth in the core of the SSGF [*Hulen and Pulka*, 2001], a quartz-dominated rheology likely cannot explain the depth distribution of

Figure 12. Cross section through the (top) geothermal anomaly and (bottom) Vp model along the same line as the InSAR data section in Figures 9 and 10. The colors denote the Vp anomaly (in km/s) relative to the starting model shown in Figure 8. The magenta circles denote the 2005 swarm events within 1 km of the cross-section line in Figure 11. The white triangles denote the fault segments from the InSAR inversion within 1 km of the cross section in Figure 11. The seismic swarm occurs directly under the high-temperature part of the geothermal field, while the aseismic fault creep occurs on the boundary between the high Vp and low Vp regions.

earthquakes, particularly in the 2005 swarm, which ruptured down to ~5 km directly in the middle of the geothermal anomaly. In general, the background seismicity occurs in the 1–2 km depth range, which corresponds to the upper reservoir layer of relatively unaltered sandstone [*Younker et al.*, 1982]. Beneath this lies a lower reservoir layer of reduced porosity, hydrothermally altered sediments that have been metamorphosed into dense, highly fractured albite-epidote hornfels [*Clayton et al.*, 1968], whose lower extent is unknown. The 2005 swarm occurred primarily in this depth range (2–5 km). Its rupture into a region with significantly higher temperatures than is typically associated with velocity-weakening behavior for sandstone likely indicates that the lower reservoir region is dominated by the frictional properties of feldspar and pyroxene, with very little quartz contamination.

Perhaps more interesting is that the apparent spatial separation between the aseismic creep and the earthquake swarm during the 2005 event almost exactly follows the geothermal reservoir boundary, indicating a first-order control of frictional stability by metamorphic composition. Figures 11 and 12 compare the location of the curved fault surface that best fits the InSAR data, with both the shallow heat flow (temperature gradient) and the *P* wave velocity in the upper reservoir layer. The aseismic creep on the Kalin fault clearly occurred outside the zone of high Vp and high temperatures, whereas the earthquake swarm on the Main Central Fault ruptured the core of the high-temperature high-Vp zone. This difference in seismogenic behavior is consistent with the Main Central Fault being dominated by the frictional properties of feldspar and pyroxene, while the Kalin fault is dominated by the frictional properties of quartz.

The large unstable creep events on faults in the Salton Trough are best explained with three-dimensional variations in frictional stability in the shallow fault zone. The Kalin fault could easily fit these criteria with a few hundred meter thick ductile cap rock layer overlying a relatively narrow depth range where the temperature is appropriate for quartz to experience velocity weakening. This type of layering could result in a thin enough velocity-weakening zone to enable large creep events as seen in numerical models that incorporate short length-scale variations in the rate-state friction properties of the shallow fault zone [*Wei et al.*, 2013].

4.4. Interactions Between Induced Seismicity and the Tectonic Fault System

Our earthquake relocations reveal complex interactions between the microseismicity induced by geothermal operations and the large-scale tectonic faults. It is well known that the seismicity within the SSGF has repeated earthquake swarms that migrate spatially and indicate periods of increased stressing-rate that likely result from a combination of aseismic fault motion and fluid migration [*Llenos et al.*, 2009; *Chen and Shearer*, 2011; *Llenos and McGuire*, 2011], but the extent to which seismicity involves the preexisting tectonic faults has been unclear. The ubiquity of faults in the reflection sections both onshore [*Catchings et al.*, 2010] and offshore [*Brothers et al.*, 2011] near the SSGF indicates that there is likely to be a connection between these existing structures and the seismicity induced by the geothermal operations. The 2008–2012 microseismicity was concentrated in two clear clusters at the NE and SW ends of the Main Central Fault zone, each of which is located near a group of injection wells (white circles in Figure S1). The seismicity in each of these clusters does not collapse onto a simple fault, rather the SE cluster has a diameter of about 2 km in map view and the NE
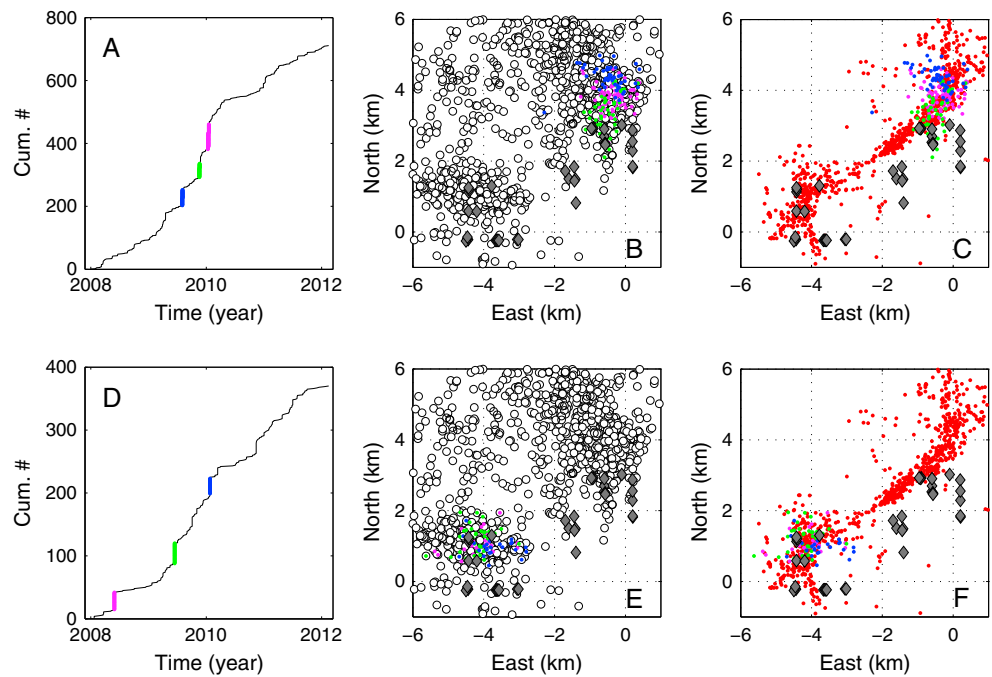
Figure 13. (a) Cumulative number of earthquakes versus time in the relocated catalog for the northwestern cluster of seismicity related to the geothermal field operation. Three-day long swarms of earthquakes are highlighted in blue, green, and magenta. (b) Map view showing the relocated 2008–2012 seismicity (white circles), the injection wells (gray diamonds), and the location of the three swarms in Figure 13a (same colors as Figure 13a). (c) Locations of the 2005 earthquake swarm (red dots), the injection wells (gray diamonds), and the three swarms in Figure 13a (same colors as Figure 13a). (d–f) Similar plots as Figures 13a–13c, respectively, showing the three largest clusters in the southeastern cluster of seismicity. In both the northeastern and southwestern clusters of seismicity, earthquake swarms preferentially occur along the bends in the Main Central Fault, as compared to the wider cloud of nominally induced seismicity. As in Figure 8, it is possible that our earthquake relocations are biased ~500 m too far north relative to the well locations. Also, not all wells are vertical (Figure 3), so their surface locations do not necessarily indicate their intersection with the Main Central Fault.

cluster has a diameter of about 4 km. In both clusters, seismicity is concentrated in the depth range from 1 to 3 km, consistent with the typical well depths in the SSGF (Figure 3).

While the general background seismicity does not collapse to the Main Central Fault of *Hulen et al.* [2003], the earthquake swarms do. Figures 13a and 13d show the temporal history of our relocated catalog (roughly $M > 1$) from 2008 to 2012 for the NE and SW clusters, respectively. While there is a fairly constant background rate in both clusters, there are several swarms of microearthquakes that make up a significant fraction (~1/4) of the total seismicity. For each cluster, we have highlighted the three biggest swarms with a different color. Figures 13b and 13e show epicenters of these swarms plotted on top of the 2008–2012 background seismicity for the NE and SW clusters, respectively. The swarms are clearly concentrated in a small region of the overall cluster that is closest to the injection wells. Figures 13c and 13d show the same swarms plotted on top of our relocations for the 2005 swarm. The 2008–2012 swarms in both the SE and NW clusters are coincident with and contained within the bends at each end of the Main Central Fault.

Given the immense amount of fluid injection into a plate boundary fault system (about 1×10^6 m^3/month for the last 25 years) [*Brodsky and Lajoie*, 2013], the SSGF makes a natural area to investigate induced seismicity. Recently, *Brodsky and Lajoie* [2013] used statistical modeling of the seismicity in the SSGF to examine the connections between the geothermal operations and potential earthquakes on natural faults including the nearby San Andreas. They found that there was no significant correlation between the time histories of any of the operational parameters (amount of fluid produced, amount injected, or net production = production reinjection) with the background seismicity rate variations for the time period from 1991 to 2006. However, from 2006 to 2012, there was a moderate correlation with net production. While they did not address it directly, the obvious question is what changed around 2006 to cause the increase in this correlation? While there was a change in the data loggers used to record the injection and extraction data during 2006, there
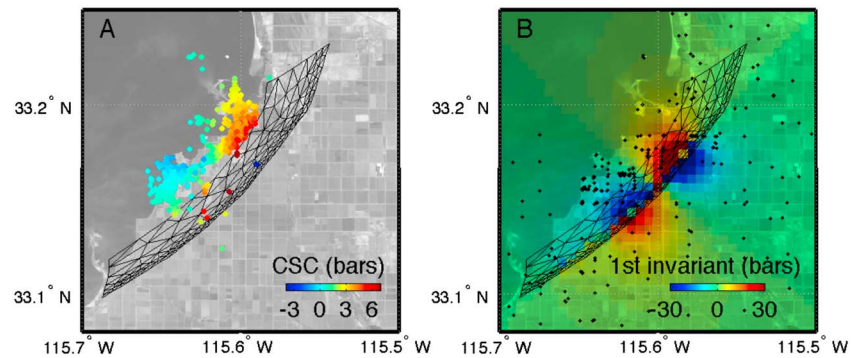
Figure 14. Expected static stress changes due to inferred deformation during 2005 aseismic slip event. (a) Expected static Coulomb stress change for each of the earthquakes that occurred during the swarm, assuming the fault plane orientation of the largest *Mw* 5.1 event, and (b) the first invariant of stress tensor at 2 km depth.

are observations of changes in earthquake behavior at this time that are not dependent on the well data. *Llenos and Michael* [2014] also document a change in the earthquake clustering behavior, namely a decrease in the productivity of aftershocks, around the time of the 2005 swarm. Both studies may indicate a connection between the sensitivity of earthquake triggering to the stress perturbations produced within the SSGF by the 2005 swarm. At least two physical mechanisms are plausible for creating such a change after 2005. First, the static deformation associated with the creep event and earthquakes may have altered the stress field in the high-seismicity regions. As an example, Figure 14 illustrates the expected static Coulomb stress change due to the inferred 2005 aseismic slip event at the locations of swarm seismicity (Figure 14a), and the first invariant of stress at 2 km depth (Figure 14b) across the SSGF as a whole. While the timing of the aseismic slip relative to the swarm seismicity is not well defined [*Lohman and McGuire*, 2007], the expected stress changes are consistent with the area where the swarm initiated (NE). Moreover, the overall increase in the first invariant of the stress tensor may have brought the more distributed network of fractures that is responsible for the bulk of microseismicity, closer to failure. This may be the underlying cause of the observed changes in earthquake-triggering statistics following the 2005 swarm. Second, the actual fault slip along the Main Central Fault during the 2005 swarm may have increased the permeability of that fault zone, allowing a more direct connection between the well operations and earthquake swarms.

The extent to which the induced seismicity in the SSGF creates an increase in the larger-scale earthquake hazard in the region is an open question. All of the $M > 4.0$ earthquakes in the SSGF since 2000 occurred during the 2 day period of the 2005 swarm and were located within the Main Central Fault zone. Our inference that the metamorphic reactions associated with the geothermal anomaly significantly modify the frictional stability of the shallow Salton Trough sediments indicates that the maximum magnitude of induced seismicity is likely to be controlled in part by the spatial extent (area) of the faults within the high heat flow zone. Moreover, whereas the background seismicity is spread over a wider region, the clustered part of the seismicity, in which most moderate earthquakes occur, is clearly very tightly controlled by the preexisting structure of the Main Central Fault. This was true in both the very large 2005 swarm as well as in the smaller swarms from 2008 to 2012 (Figure 13). The seismicity rate in these clusters does not decay with distance in a radially symmetric way, and the use of stochastic models that model the spatial decay of clustered earthquakes with radially symmetric expressions [*Lajoie*, 2012] may improperly extrapolate the expected rate increase during seismicity clusters (swarms/aftershocks). In particular, the swarms clearly migrate along the fault, sometimes at relatively fast velocities (~0.5–1 km/h) [*Lohman and McGuire*, 2007] and sometimes at slower more fluid diffusion-like speeds [*Chen and Shearer*, 2011]. Both types of swarms appear to indicate a specific physical process such as fault creep and/or fluid migration that primarily trigger earthquakes on the Main Central Fault, owing to the need for either aseismic slip or fluid to propagate within the fault zone. As this appears to be the dominant effect on the temporally clustered seismicity within the field, extrapolating a radially symmetric distance falloff for these clusters, which does not mimic the fault structure, would likely be biased toward overestimating the rate of earthquakes that can be triggered far off of the Main Central Fault. Future statistical studies that examine the difference in clustering properties of swarms on the MCF compared to the background seismicity will be very valuable. If there is a significant

potential for the microearthquakes in the SSGF to trigger a larger rupture, it would likely involve a failure of the entire Main Central Fault. The 2005 earthquake swarm migrated across the ~10 km span of the Main Central Fault, but its largest earthquake was only magnitude 5.1. It is possible that MCF, which has a very complicated thermomechanical environment, may be capable of larger M5.5–6 ruptures. Improved paleoseismic studies of the MCF would be a valuable contribution to understanding the likely maximum magnitude of earthquakes triggered within the SSGF.

5. Conclusions

There are strong velocity variations in P wave velocity within the SSGF, up to ~30%, that correlate spatially with the distribution of shallow heat flow anomalies. The combination of hydrothermal circulation and high-temperature contact metamorphism has significantly altered the shallow sandstone sedimentary layers within the geothermal field to denser, more feldspathic, rock with higher P wave velocity as is seen in the numerous exploration wells within the field. This alteration appears to have a first-order effect on the frictional stability of shallow faults. The shallow aseismic fault creep that occurred in 2005 was localized on the Kalin fault, which lies just outside the region of high-temperature metamorphism. In contrast, the earthquake swarm, which includes all of the $M > 4$ earthquakes that have occurred within the SSGF in the last 15 years, ruptured the Main Central Fault that is localized in the heart of the geothermal anomaly. The background microseismicity apparently induced by the geothermal operations is also concentrated in the high-temperature regions in the vicinity of operational wells. However, while this microseismicity occurs over a scale of a few kilometers, much of it is clustered in earthquake swarms that last from hours to a few days and are localized to the Main Central Fault. The Main Central Fault appears to be the dominant structure in the SSGF capable of generating significant earthquakes. It is currently unclear whether the Main Central Fault could generate a larger earthquake than those that occurred in the 2005 swarm. Whereas its ~10 km length would suggest the possibility of $\underline{M} \sim 5.5$–6 earthquakes, the rapid spatial variations in lithology and thermal structure may limit the seismic potential of this fault. An improved understanding of the paleoseismic history of the Main Central Fault, as well as a better understanding of the connections between geothermal operations and the swarms on the MCF, both needed to help clarify the seismic hazard in the region.

References

Bilham, R., N. Suszek, and S. Pinkney (2004), California creepmeters, *Seismol. Res. Lett.*, *75*(4), 481–492.

Blanpied, M. L., D. A. Lockner, and J. D. Byerlee (1991), Fault stability inferred from granite sliding experiments at hydrothermal conditions, *Geophys. Res. Lett.*, *18*(4), 609–612, doi:10.1029/91GL00469.

Bodin, P., R. Bilham, J. Behr, J. Gomberg, and K. W. Hudnut (1994), Slip triggered on southern California faults by the 1992 Joshua-Tree, Landers, and Big-bear earthquakes, *Bull. Seismol. Soc. Am.*, *84*(3), 806–816.

Brodsky, E. E., and L. J. Lajoie (2013), Anthropogenic seismicity rates and operational parameters at the Salton Sea Geothermal Field, *Science*, *341*(6145), 543–546.

Brothers, D., D. Kilb, K. Luttrell, N. Driscoll, and G. Kent (2011), Loading of the San Andreas fault by flood-induced rupture of faults beneath the Salton Sea, *Nat. Geosci.*, *4*(7), 486–492.

Brune, J. N., and C. R. Allen (1967), A low stress-drop low-magnitude earthquake with surface faulting—Imperial California Earthquake of March 4 1966, *Bull. Seismol. Soc. Am.*, *57*(3), 501–514.

Catchings, R. D., M. J. Rymer, M. D. Goldman, R. B. Lohman, and J. J. McGuire (2010), The Obsidian Creep Project: Seismic Imaging in the Brawley Seismic Zone and Salton Sea Geothermal Field, Imperial County, California, Abstract T53B-2122 presented at 2010 Fall Meeting, AGU, San Francisco, Calif., 13–17 Dec.

Chen, X., and P. M. Shearer (2011), Comprehensive analysis of earthquake source spectra and swarms in the Salton Trough, California, *J. Geophys. Res.*, *116*, B09309, doi:10.1029/2011JB008263.

Clayton, R. N., L. J. P. Muffler, and D. E. White (1968), Oxygen isotope study of calcite and silicates of the River Ranch No. 1 Well, Salton Sea Geothermal Field, California, *Am. J. Sci.*, *266*, 968–979.

Crowell, B. W., Y. Bock, D. T. Sandwell, and Y. Fialko (2013), Geodetic investigation into the deformation of the Salton Trough, *J. Geophys. Res. Solid Earth*, *118*, 5030–5039.

Daley, T. M., T. V. McEvilly, and E. L. Majer (1988), Analysis of P-wave and S-wave vertical seismic profile data from the Salton-Sea_Scientific-Drilling-Project, *J. Geophys. Res.*, *93*(B11), 13,025–13,036, doi:10.1029/JB093iB11p13025.

Elders, W. A., and J. H. Sass (1988), The Salton Sea Scientific Drilling Project, *J. Geophys. Res.*, *93*, 12,953–12,968, doi:10.1029/JB093iB11p12953.

Eneva, M., and D. Adams (2010), Modeling of surface deformation from satellite radar interferometry in the Salton Sea Geothermal Field, California, *Geoth. Resour. Counc. Trans.*, *34*, 527–534.

Fialko, Y., D. Sandwell, M. Simons, and P. Rosen (2005), Three-dimensional deformation caused by the Bam, Iran, earthquake and the origin of shallow slip deficit, *Nature*, *435*, 295–299.

Hauksson, E., et al. (2013), Report on the August 2012 Brawley Earthquake Swarm in Imperial Valley, Southern California, *Seismol. Res. Lett.*, *84*(2), 177–189.

He, C. R., Z. L. Wang, and W. M. Yao (2007), Frictional sliding of gabbro gouge under hydrothermal conditions, *Tectonophysics*, *445*(3–4), 353–362.

He, C. R., L. Luo, Q. M. Hao, and Y. S. Zhou (2013), Velocity-weakening behavior of plagioclase and pyroxene gouges and stabilizing effect of small amounts of quartz under hydrothermal conditions, *J. Geophys. Res. Solid Earth*, *118*, 3408–3430.

Hulen, J. B., and F. S. Pulka (2001), Newly-discovered, ancient extrusive rhyolite in the Salton Sea Geothermal Field, Imperial Valley, California, paper presented at Twenty-Sixth Workshop on Geothermal Reservoir Engineering, Stanford Univ., Stanford, Calif.

Hulen, J. B., D. Kaspereit, D. Norton, W. Osborn, and F. S. Pulka (2002), Refined conceptual modeling and a new resource estimate for the Salton Sea Geothermal Field, Imperial Valley, CA, *Geoth. Resour. Counc. Trans.*, *26*, 29–36.

Hulen, J. B., D. Norton, D. Kaspereit, L. Murray, T. van de Putte, and M. Wright (2003), Geology and a working conceptual model of the Obsidian Butte (Unit 6) sector of the Salton Sea Geothermal Field, California, *Geoth. Resour. Counc. Trans.*, *27*, 227–240.

Johnson, C. E., and D. M. Hadley (1976), Tectonic implications of Brawley earthquake swarm, Imperial-Valley, California, January 1975, *Bull. Seismol. Soc. Am.*, *66*(4), 1133–1144.

Lajoie, L. J. (2012), Seismic response to fluid injection and production in two Salton Trough geothermal fields, southern California, Master's thesis, Univ. of Calif. Santa Cruz, Santa Cruz.

Lin, G., P. M. Shearer, and E. Hauksson (2007), Applying a three-dimensional velocity model, waveform cross correlation, and cluster analysis to locate southern California seismicity from 1981 to 2005, *J. Geophys. Res.*, *112*, B12309, doi:10.1029/2007JB004986.

Llenos, A. L., and A. J. Michael (2014), Characterizing potentilly induced earthquake rate changes in the Brawley Seismic Zone, CA, *Seismol. Res. Lett.*, *85*(2), 488.

Llenos, A. L., and J. J. McGuire (2011), Detecting aseismic strain transients from seismicity data, *J. Geophys. Res.*, *116*, B06305, doi:10.1029/2010JB007537.

Llenos, A. L., J. J. McGuire, and Y. Ogata (2009), Modeling seismic swarms triggered by aseismic transients, *Earth Planet. Sci. Lett.*, *281*(1–2), 59–69.

Lohman, R. B., and J. J. McGuire (2007), Earthquake swarms driven by aseismic creep in the Salton Trough, California, *J. Geophys. Res.*, *112*, B04405, doi:10.1029/2006JB004596.

Lovely, P., J. H. Shaw, Q. Liu, and J. Tromp (2006), A structural Vp model of the Salton Trough, California and its implications for seismic hazard, *Bull. Seismol. Soc. Am.*, *96*(5), 1882–1896.

Lyons, S., and D. Sandwell (2003), Fault creep along the southern San Andreas from interferometric synthetic aperature radar, permanent scatterers, and stacking, *J. Geophys. Res.*, *108*(B1), 2047, doi:10.1029/2002JB001831.

Marone, C. J. (1998), Laboratory-derived friction laws and their application to seismic faulting, *Annu. Rev. Earth Planet. Sci.*, *26*, 643–696.

Marone, C. J., C. H. Scholtz, and R. Bilham (1991), On the mechanics of earthquake afterslip, *J. Geophys. Res.*, *96*(B5), 8441–8452, doi:10.1029/91JB00275.

Newmark, R. L., P. W. Kasameyer, L. W. Younker, and P. Lysne (1988), Shallow drilling in the Salton Sea region—The thermal anomaly, *J. Geophys. Res.*, *93*, 13,005–13,023, doi:10.1029/JB093iB11p13005.

Richter, C. F. (1958), *Elementary Seismology*, W. H. Freeman, San Fransisco, Calif.

Roland, E., and J. J. McGuire (2009), Earthquake swarms on transform faults, *Geophys. J. Int.*, *178*(3), 1677–1690.

Rose, E. J., et al. (2013), Borehole-explosion and air-gun data acquired in the 2011 Salton Seismic Imaging Project (SSIP), southern California—Description of the survey, *U.S. Geol. Surv. Open File Rep.*, *2013–1172*, 84 p.

Rymer, M. J., et al. (2010), Triggered surface slips in southern California associated with the 2010 El Mayor-Cucapah, Baja California, Mexico, earthquake, *U.S. Geol. Surv. Open File Rep.*, *2010–1333*, 62 p.

Scholz, C. H. (1998), Earthquakes and friction laws, *Nature*, *391*, 37–42.

Tape, C., Q. Y. Liu, A. Maggi, and J. Tromp (2009), Adjoint tomography of the Southern California crust, *Science*, *325*(5943), 988–992.

Tse, S. T., and J. R. Rice (1986), Crustal earthquake instability in relation to the depth variation of frictional properties, *J. Geophys. Res.*, *91*(B9), 9452–9472, doi:10.1029/JB091iB09p09452.

Wei, M., D. Sandwell, and Y. Fialko (2009), A silent M_w 4.7 slip event of October 2006 on the Superstition Hills fault, southern California, *J. Geophys. Res.*, *114*, B07402, doi:10.1029/2008JB006135.

Wei, M., Y. Kaneko, Y. Liu, and J. J. McGuire (2013), Episodic fault creep events in California controlled by shallow frictional heterogeneity, *Nat. Geosci.*, *6*, 566–570.

Younker, L. W., P. W. Kasameyer, and J. D. Tewhey (1982), Geological, geophysical, and thermal characteristics of the Salton Sea Geothermal Field, California, *J. Volcanol. Geoth. Res.*, *12*, 221–258.

Zhang, H., and C. Thurber (2003), Double-difference tomography: The method and its application to the Hayward fault, California, *Bull. Seismol. Soc. Am.*, *93*(5), 1875–1889.

Zhang, H., and C. Thurber (2006), Development and applications of double-difference seismic tomography, *Pure Appl. Geophys.*, *163*(2), 373–403.